Three-dimensional optical tomographic imaging of supersonic jets through inversion of phase data obtained through the transport-of-intensity equation

Hemanth Thayyullathil, Rajesh Langoju, Renganathan Padmaram, R. Mohan Vasu, Rajan Kanjirodan, and Lalit M. Patnaik

We report experimental results of quantitative imaging in supersonic circular jets by using a monochromatic light probe. An expanding cone of light interrogates a three-dimensional volume of a supersonic steady-state flow from a circular jet. The distortion caused to the spherical wave by the presence of the jet is determined through our measuring normal intensity transport. A cone-beam tomographic algorithm is used to invert wave-front distortion to changes in refractive index introduced by the flow. The refractive index is converted into density whose cross sections reveal shock and other characteristics of the flow. © 2004 Optical Society of America

OCIS codes: 100.3010, 100.3190, 100.5070, 100.6950, 170.3010, 170.6960.

1. Introduction

One of the important experimental problems in fluid mechanics is quantitative flow visualization especially of high-speed or turbulent flows or both. Probing with light is the preferred method, for an optical probe does not disturb the flow. Examples of light-based probes are the laser Doppler velocimeter and the particle image velocimeter. These methods measure the velocity vector field, pointwise by the laser Doppler velocimeter and two-dimensional (2-D) cross sections through the particle image velocimeter. The study of fluctuations of the longitudinal component of velocity has become the standard route to analyze a turbulent flow. Experimental data on fluctuations are used to verify the so-called Kolmogorov's refined self-similarity hypothesis.[1] The second quantity that is extensively studied to ascertain large-scale statistically meaningful average quantities from turbulent flows is dissipation fluctuations.[2,3] A third quantity, which is not extensively studied for the same aim, is density and its fluctuations. The reason is not hard to see: Except in certain supersonic flows, in water, and in shocks, the flow usually has no density variations. But in situations in which there is density variation, as, for example, in the mixing of a low-density fuel (such as hydrogen) in high-density oxygen, measurement of 2-D or 3-D densities and their variations in time is important, for they can be used in a way similar to velocity fluctuations, to estimate coherent structures and their dynamics in turbulent flows.

The optical technique for measurement of density distribution in flows is tomography. It was used to visualize blade-tip vortices from a helicopter in flight[4] and quantitative cross-sectional measurements in a heated round jet emitting to cold air.[5] Cross-sectional images through the flow at different downstream locations helped researchers to analyze the development of flow structure.[6] In optical tomography the travel time of a monochromatic light wave through a refractive-index distribution representing the flow is measured. An equivalent quantity, namely, phase of the wave, is measured at various angles of illumination, also called views. Phase is the so-called projection data, which are backprojected by use of standard tomographic algorithms such as the filtered backprojection or algebraic reconstruction technique.[7]

The experimental measurement part of tomographic imaging is phase- or wave-front estimation, which is traditionally done in optics through inter-

T. Hemanth (hemanth@physics.iisc.ernet.in) and K. Rajan are with the Department of Physics, Indian Institute of Science, Bangalore 560012, India. L. V. V. L. Rajesh, R. Padmaram, and R. Mohan Vasu are with the Department of Instrumentation, Indian Institute of Science. L. M. Patnaik is with the Microprocessor Applications Laboratory, Indian Institute of Science.

Received 5 September 2003; revised manuscript received 27 April 2004; accepted 3 May 2004.

0003-6935/04/214133-09$15.00/0

© 2004 Optical Society of America

ferometry.[8] Noninterferometric methods, which are robust and not sensitive to vibration, are also developed for estimating phase data for optical tomography.[5,9,10] Many of the noninterferometric methods rely on measurement of wave-front slopes with, for example, a Hartmann sensor. Others depend on complete phase reconstruction from intensity measurements through analytical as well as iterative phase-retrieval algorithms.[11–13] One of the wave-front estimation methods, based on the transport-of-intensity equation (TIE) to retrieve phase from intensity measurements,[14] has been used recently to reconstruct refractive-index cross sections of fiber in a tomographic microscope.[15,16] The advantages of the TIE-based wave-front estimation, in the context of tomographic imaging, are owed to unique (up to an arbitrary, additive constant) and unwrapped phase recovery possible from a straightforward experimental measurement of two intensities. In the present paper we use the TIE to estimate the phase of light transmitted through a supersonic jet, illuminated with a diverging cone beam. The TIE is solved with series-expansion methods[17] (Fourier harmonics when the wave front has a rectangular boundary and the Zernike polynomial for a circular boundary). The series-expansion method lends itself to an easily solvable equation under the assumption of constant transverse intensity, which we have borrowed to solve the TIE in this case. Without the assumption of constant transverse intensity, the TIE is solved with finite-element (FEM) discretization. The retrieved phase is used in direct 3-D reconstruction of refractive index with a standard cone-beam algorithm.[18] The reconstructed refractive index is converted into density with the Gladstone–Dale equation.[19]

The organization of the rest of the paper is as follows. In Section 2 we describe phase retrieval through solving the TIE by using both Fourier harmonic expansion[17] and FEM discretization. In Section 3 the 3-D cone-beam reconstruction algorithm, which we have used in this paper, is described in some detail. Section 4 deals with the description of experiments done on a supersonic flow from a round jet. The data gathered are used in the TIE, and the retrieved wave front on display gives a visualization of the flow in which the internal structures are quite discernible. The estimated wave front is input to a tomographic reconstruction algorithm, and the cross sections of the reconstructed density distributions are presented and described. Section 5 describes in detail the results of density reconstruction. Finally, Section 6 gives our concluding remarks.

2. Phase Reconstruction with the Transport-of-Intensity Equation

The TIE is a coupled partial differential equation connecting axial transport of intensity $\partial I/\partial z$ to the phase $\phi(x, y)$ across the transverse X–Y plane, which was first applied to phase retrieval by Teague.[20] The TIE is valid only under paraxial approximation to light propagation, which would mean that complex amplitude $\tilde{u}(x, y, z)$ of monochromatic light could be approximated by

$$\tilde{u}(x, y, z) = u(x, y, z)\exp(jkz),$$

with $u(x, y, z)$ given by

$$I_z(x, y)^{1/2} \exp[j\phi(x, y)]$$

and $I_z(x, y) = I(x, y, z)|_{z=\bar{z}}$, the intensity distribution in the transverse plane X–Y. The TIE is

$$k\frac{\partial I}{\partial z} = -\nabla \cdot (I\nabla\phi), \tag{1}$$

where ∇ is the 2-D gradient operator. Equation (1) is solved with either the Dirichlet or the Neumann boundary conditions. Vdovin[21] has attempted a direct (i.e., strong) solution to Eq. (1) by discretizing the partial differential equation by using the finite-difference method. Many others attempted a weak solution to Eq. (1) with such test function spaces as Fourier harmonics[17] and Zernike polynomials.[14] Using Fourier harmonics expansion, suited when the domain is rectangular (for example, when a rectangular CCD array is used to gather intensity data), Gureyev and Nugent[17] have shown that Eq. (1) can be converted into a set of linear algebraic equations given by

$$\sum_{i,j} \Phi_{ij} A_{mn}^{\ ij} = abD_{mn}, \tag{2}$$

where D_{mn} is the projection of

$$D = k(\partial I/\partial z),$$

by using the kernel

$$W_{mn} = \exp\left(\frac{j2\pi mx}{a}\right)\exp\left(\frac{j2\pi ny}{b}\right),$$

$$A_{mn}^{\ ij} = (2\pi)^2\left(\frac{imb}{a}\right)\left(\frac{ina}{b}\right)\hat{I}_{m-i,n-j},$$

where $a \times b$ is the rectangular domain under consideration and $\hat{I}_{mn} = \langle I, W_{mn}\rangle$. Similarly, $\Phi_{ij} = \langle\phi, W_{ij}\rangle$. Equation (2) can be inverted for Φ_{ij} by use of

$$\Phi_{ij} = ab\sum_{m,n}[A_{mn}^{\ ij}]^{-1}D_{mn}. \tag{3}$$

Invertibility of the matrix $[A_{mn}^{\ ij}]$ was verified,[17] but the procedure is expensive in terms of computation time. The above inversion procedure can be considerably simplified if we can assume that the transverse intensity is a constant in the domain of the problem. With $I(x, y) = I_0$, we can simplify Eq. (1) as

$$\nabla^2\phi = -\frac{k}{I_0}\frac{\partial I}{\partial z}, \tag{4}$$

and Eq. (3) simplifies to

$$\Phi_{ij} = \frac{(ab)^2}{(2\pi)^2(i^2b^2 + j^2a^2)I_0}D_{i,j}. \tag{5}$$

The above simplification of treating $I(x, y)$ as a constant cannot be justified and can lead to error and averaging in the reconstructed phase. To have a faster reconstruction of the phase without the restrictive assumption of constant transverse intensity, we can use a FEM to solve the TIE. The boundary conditions used are either Dirichlet (or extended Dirichlet[22]) or Neumann. In the FEM approach we seek a continuous piecewise linear approximation, ϕ^p, to the unknown phase $\phi(x, y)$. The problem domain Ω is divided into elements (the simplest is triangular) that are joined at nodes, ϕ^p is a linear approximation to $\phi(x, y)$, and $\phi^p(r)$ at any point r inside the element can be found by interpolation of nodal values, Φ_j.

For a particular element e_j,

$$\phi^p(r) = \sum_{i \forall \text{nodes} \in e_j} \Phi_i \Psi_i(r), \tag{6}$$

where $\Psi_i(r)$ are nodal shape functions.[22] The weak formulation of Eq. (1) by use of Galerkin's method requires the inner products of the residuals $R[=k(\partial I/\partial z) + \nabla \cdot (I \nabla \phi^p)]$ with the same basis functions to vanish. For example,

$$\sum_j \Phi_j \int_\Omega \nabla \cdot [I \nabla \Psi_j(r)] \Psi_i(r) \mathrm{d}\Omega + \int_\Omega k \frac{\partial I}{\partial z} \Psi_i(r) \mathrm{d}\Omega = 0; \qquad i, j = 1, 2, \ldots N, \tag{7}$$

where N is the number of nodes.

With the Dirichlet boundary condition, Eq. (7) can be written as a linear system of equations, which in matrix form is

$$K(I)\phi = S, \tag{8}$$

where

$$K_{i,j} = \int_\Omega I \nabla \Psi_i(r) \cdot \nabla \Psi_j(r) \mathrm{d}r,$$

$$S_i = \int_\Omega k \frac{\partial I}{\partial z} \Psi_i(r) \mathrm{d}\Omega,$$

$$\phi = [\Phi_1, \Phi_2, \ldots, \Phi_N]^T$$

is the values of ϕ at the N nodes in the domain. Equation (8) is inverted for ϕ. In this paper we have formulated Eq. (8) with the help of the MATLAB partial differential equation toolbox and solved for ϕ, and $\phi(x, y)$ is obtained through interpolation. Here $I(x, y)$ is not assumed constant. With the simplifying assumption of I = constant, Eq. (5) was used to solve for $\Phi_{i,j}$, the Fourier coefficients of $\phi(x, y)$.

3. Cone-Beam Tomographic Reconstruction of a Three-Dimensional Refractive Index from the Phase Data

The phase data calculated with the TIE is the projection data, from which the refractive-index distribution, which is the flow, can be reconstructed. A collection of line integrals through $n(x, y, z)$, the 3-D refractive-index distribution, represents a view resulting in 2-D optical path (or projection) data.

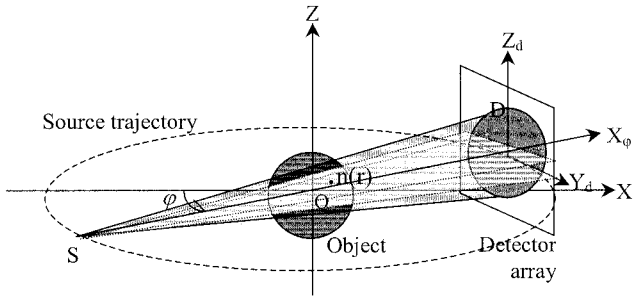

Fig. 1. Geometry used in the Feldkamp–Davis–Kress cone-beam reconstruction algorithm. S is the source that illuminates the object whose center is at O, the origin of the coordinate system. The source trajectory is shown as a dotted circle around the object. Data collection on the detector array at a view angle φ is schematically shown. The axis of the cone at this view is shown as X_φ. The coordinates of any point on the detector system are (Y_d, Z_d).

An optical path along a ray, $\delta(\mathbf{t} - \mathbf{x} \cdot \boldsymbol{\xi})$, is given by (Fig. 1)

$$P(t, \boldsymbol{\xi}) = \iiint n(\mathbf{x}) \delta(t - \mathbf{x} \cdot \boldsymbol{\xi}) \mathrm{d}\mathbf{x}, \tag{9}$$

where $\mathbf{x}$ is the position vector (x, y, z) and

$$\boldsymbol{\xi} = (\sin\theta \cos\phi, \sin\theta \sin\phi, \cos\theta).$$

Here the light is assumed to travel along straight lines, which is not strictly valid because of refraction caused by density gradients in the flow. Refraction correction is incorporated in 2-D optical tomographic algorithms[23] and is considered necessary when density gradients are large. Because of the enormous computation time involved, to the best of our knowledge, refraction-corrected 3-D algorithms are not yet popular. In the present paper also, which attempts 3-D reconstruction, refraction is ignored at the expense of accuracy.

In x-ray tomography, the parallel-beam 3-D reconstruction problem is divided into a number of 2-D problems; the 2-D reconstructions are stacked to form a 3-D image. Stacking adversely affects the resolution in the direction of stacking in that light propagation is truly 3-D and cannot be confined to a plane. Because 2-D reconstructions in optical tomography are inherently defective, in this paper we attempt 3-D reconstructions by using the so-called cone-beam data. The cone beam has an additional advantage in that an expanding cone of light easily covers a larger volume of the object. In this sense, cone-beam tomography is an extension to three dimensions of the well-known 2-D fan-beam tomography.[24] A line-integral travel-time data set is obtained on a divergent set of rays coming from a cone vertex. In cone-beam tomography this diverging line-integral data set (or cone-beam data) is inverted to get back a 3-D refractive-index distribution.

The simplest and computationally most efficient

algorithm to invert cone-beam data is from Feldkamp, Davis, and Kress[18] (FDK) in which the vertex of the cone moves along a circle. The data from the circular path are, however, incomplete for exact 3-D reconstruction,[25] except for one cross section of the object containing the circle. The two drawbacks pointed out in Ref. 26 are (1) the density resolution of the FDK algorithm is poorer compared with a usual 2-D algorithm and (2), for large cone angles, the reconstructions are severely prone to errors.

Tuy,[27] and, independently, Smith,[26] gave vertex paths, which satisfy data sufficiency conditions for getting more accurate cone-beam reconstructions. Whereas the FDK algorithm uses a one-dimensional ramp filter on the data followed by backprojection (retaining the spirit and the simplicity of a 2-D filtered backprojection algorithm), the modified algorithms are based on a 2-D space-variant filtering of cone-beam data prior to backprojection.[28] Kudo and Saito[25] decomposed the complete vertex path into circle(s), and, for the circles, a one-dimensional ramp filter of the FDK algorithm is retained. To ensure that the filtered data have no singularities, Noo *et al.*[29] modified Kudo and Saito's method so that the circle data are filtered by a 2-D space-invariant filter. These modified algorithms gave superior results when applied to simulated projection data.

In the present paper we have used the computationally simple FDK algorithm. The modifications of Refs. 28 and 29 are being implemented, and the improved reconstructions from experimental data are set apart for future publications. The summary of the FDK algorithm is given below.

As already mentioned, for the FDK algorithm, the source trajectory is a circle that surrounds the object (Fig. 1). A number of projections are obtained on the detector plane for different locations of the source vertex. The FDK algorithm implements a number of generalized fan-beam filtered backprojections, after dividing the cone-beam data into sets of fan-beam data. In the FDK algorithm, only that cross section of the object that contains the source trajectory is reconstructed with the best possible accuracy. As one moves away from this plane into other tilted fan beams, the reconstruction error for those cross sections increases.

The formula used in the FDK algorithm to reconstruct the refractive-index distribution $n(\mathbf{r})$ from the optical path delay data, $P_\varphi[Y_d(\mathbf{r}), Z_d(\mathbf{r})]$, is given by (Fig. 1)

$$n(\mathbf{r}) = \frac{1}{4\pi^2}\oint \frac{SO^2}{(SO + \mathbf{r}\cdot\hat{\mathbf{x}}_\varphi)^2}\tilde{P}_\varphi[Y_d(\mathbf{r}), Z_d(\mathbf{r})]\mathrm{d}\varphi. \tag{10}$$

Here $\tilde{P}_\varphi$ are the scaled and filtered optical path values for a view angle φ. Scaling of the optical path is done by multiplication of a geometric factor SO/SD, where SO is the distance between the source and the object center and SD is the distance from the source to the respective detector points. Filtering is done along the rows of the projection data with the Shepp–Logan filter.[30] The unit vector $\hat{\mathbf{x}}_\varphi$ is along the rotated X axis (shown as $\mathbf{X}_\varphi$ in Fig. 1), and $\mathbf{r}$ is the position vector of the point at which the refractive index $n(\mathbf{r})$ is calculated. The detector coordinates are $Y_d(\mathbf{r})$ and $Z_d(\mathbf{r})$, where $\mathbf{r}$, the position vector of a typical point in the object, is explicitly shown in Fig. 1 to indicate the contribution of data to the reconstruction of the object refractive index at $\mathbf{r}$.

The algorithm has three main steps: (1) scaling the optical path difference data, (2) one-dimensional ramp filtering, and (3) 3-D backprojection after a second scaling {by factor $SO^2/[(SO + \mathbf{r}\cdot\hat{\mathbf{x}}_\varphi)^2]$}.

Further details of the implementation of the FDK algorithm can be found in Refs. 7 and 18.

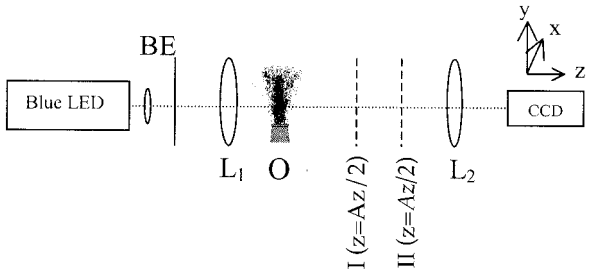

Fig. 2. Experimental setup used for recording transmitted intensity. Light from a blue LED (λ = 474 nm) is expanded by use of a beam expander (BE), and, by the suitable positioning of the lens L_1, a cone beam of the required radius of curvature is obtained, which illuminates the object O. The intensity distribution at two planes marked as I and II are recorded on the CCD with the help of lens L_2.

4. Experiment

A. Imaging Assembly

The object, which is an expanding supersonic jet of nitrogen into atmosphere, was illuminated by a cone beam of light. The experimental setup is shown in Fig. 2.

Monochromatic light from a blue LED (λ = 474 nm) is expanded and collimated with a collimating lens L_1. By moving the lens toward the beam expander, we obtained a suitably expanding cone beam to illuminate the object O. The lens L_2 is an auxiliary lens, which, along with the imaging lens of the CCD camera, images the plane I immediately behind the object, which is designated as plane $z = -\Delta z/2$. The CCD camera is in a translational stage through which it can be moved axially for imaging a plane at $z = \Delta z/2$ (designated plane II), behind the first plane $z = -\Delta z/2$. We used a grating at $z = 0$ to effectively focus the CCD camera onto this plane, which was subsequently removed during data collection.

B. Description of the Flow

An overexpanded supersonic jet of nitrogen flowing into the atmosphere produced significant density gradients downstream, with a number of axially symmetric shock-cell structures. The gas at pressure 4×10^6 Pa is expanded by use of a convergent–

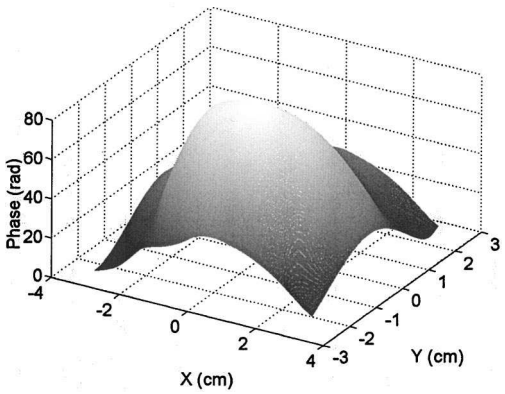

Fig. 3. Surface plot of the phase data obtained for a spherical wave front in the absence of the flow. These data are also used for calculating the radius of curvature of the spherical wave front.

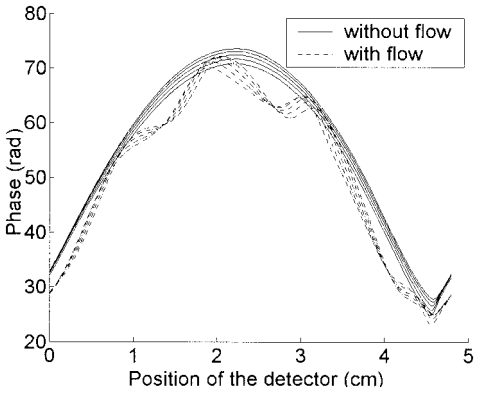

Fig. 5. Some typical cross sections of the phase profile with and without flow. Change in the wave front due to the introduction of the flow is clearly seen.

divergent nozzle with a throat diameter of 5 mm and an exit diameter of 10 mm, which resulted in nitrogen exiting the nozzle at supersonic velocities (Mach number approximately 2.9). The overexpanded jet has characteristic diamondlike shock structures with axially symmetric discs separating them. The objective of the imaging system is to get quantitative estimation of the density in these structures.

C. Description of the Experiment

To generate a cone beam to illuminate the flow, we move the collimating lens L1 (Fig. 2) away from its position of collimation, toward the source. A spherical beam of radius of curvature 29.3 cm falls on plane I ($z = -\Delta z/2$). This is experimentally verified by our reconstructing the wave front in the absence of the object (Fig. 3). Two intensities were captured, one at plane I and the other at plane II ($z = \Delta z/2$), first with the flow and then without the flow. The axial derivative of intensity $\partial I/\partial z$ is calculated as

$$\frac{I(x, y, \Delta z/2) - I(x, y, -\Delta z/2)}{\Delta z},$$

and the average intensity is calculated as

$$\frac{I(x, y, \Delta z/2) + I(x, y, -\Delta z/2)}{2}.$$

We plugged the collected data I and $\partial I/\partial z$ into the TIE [Eq. (1)] and solved for the phase $\varphi(x, y)$, by considering first that $I(x, y)$ is constant [i.e., by using Eq. (5)] and then by using the FEM without the restrictive assumption of constant transverse intensity. The distorted wave front coming through the object is also reconstructed. The distorted wave front is shown in Fig. 4. Some typical cross sections of the reconstructed phase (or wave front) obtained with and without flow are shown in Fig. 5. From the reconstructed phase distributions, $\varphi_0(x, y)$ for the background and $\varphi(x, y)$ when the object (i.e., the flow) is present, the differential phase change introduced by the flow $\Delta\varphi(x, y)$ is evaluated. The intensity image of $\Delta\varphi(x, y)$, which provides a qualitative visualization of the flow, is shown in Fig. 6. It should be pointed out that the retrieved phase from the TIE is already unwrapped and is correct within an arbitrary constant. The way to ascertain this constant is through *a priori* specifying phase at the boundaries.

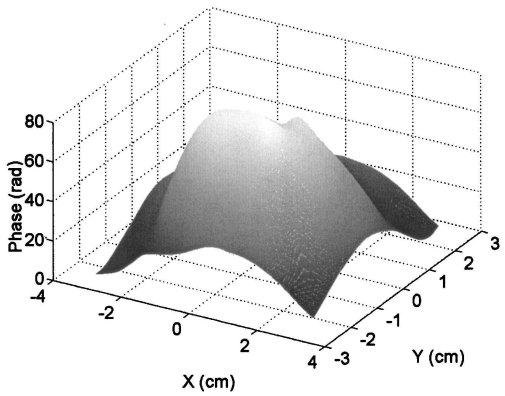

Fig. 4. Surface plot of the transmitted wave front reconstructed after the flow is introduced.

5. Results and Discussion

The simplifying assumption we make in the reconstruction is that flow from the round jet has cylindrical symmetry so that we can work with one projection data set, representative of all projections when the cone vertex moves in a circle around the flow. The

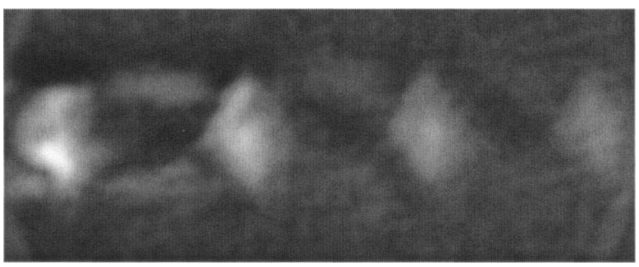

Fig. 6. Intensity image of the differential phase change.

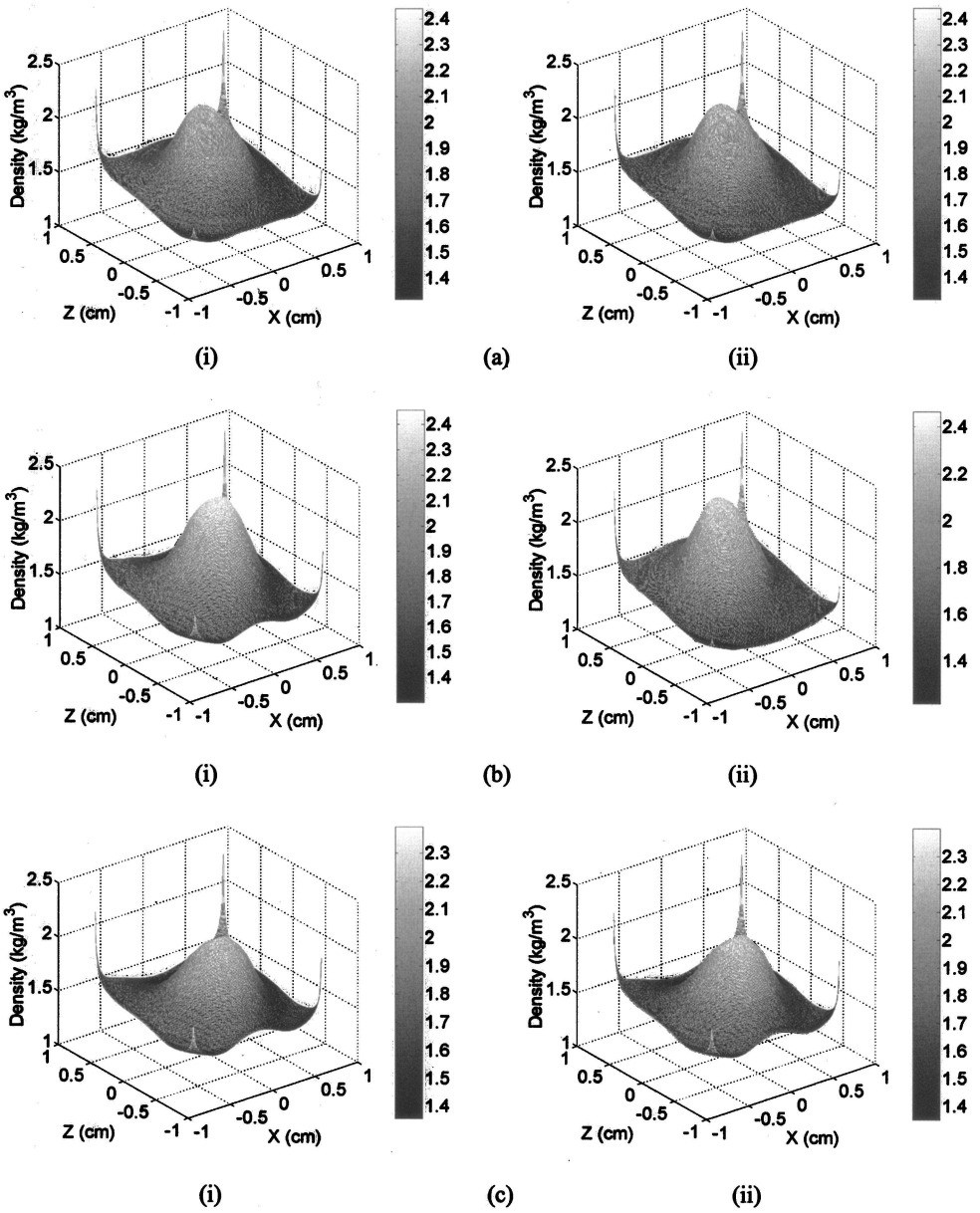

Fig. 7. Reconstructed density distributions in the X–Z planes at distances (y) from the nozzle tip: (a) $y = 0.436$ cm, (b) $y = 1.823$ cm, and (c) at $y = 3.211$ cm. Data obtained from the phase reconstructed, (i) assuming I = constant and (ii) without the assumption of constant intensity.

differential phase $\Delta\varphi$ reconstructed is assumed to be zero in the background, which is unaffected by the flow. The reconstructed $\Delta n(r)$ is added to the refractive index of air at the ambient temperature, 28 °C ($n_{\text{air}(28\,^\circ\text{C})} = 1.00028$), to get the refractive-index distribution $n(r)$ of the flow. The $n(r)$ is converted into density $\rho(r)$ with the Gladstone–Dale equation[19]:

$$\frac{(n-1)}{\rho} = G(\lambda), \tag{11}$$

where

$$G(\lambda) = 2.2244 \times 10^{-4}\left[1 + \left(\frac{6.7132 \times 10^{-2}}{\lambda}\right)^2\right],$$

ρ is in kilograms per cubic meter, and λ is the wavelength of light used in micrometers.

Typical axial cross sections (i.e., X–Z planes) of the density distributions, which are taken approximately at the centers of the first three shock cells, i.e., (a) $y = 0.436$ cm, (b) $y = 1.823$ cm, and (c) $y = 3.211$ cm, are shown in Fig. 7. Column (i) corresponds to phase data recovered assuming uniform transverse intensity, and column (ii) corresponds to phase data recovered without the assumption of uniform intensity. The maximum density in the shock cells drops as the flow goes away from the nozzle tip, and the shock cells gradually disappear.

The longitudinal cross sections (i.e., X–Y planes) are shown in Fig. 8, giving, as before, densities (col-

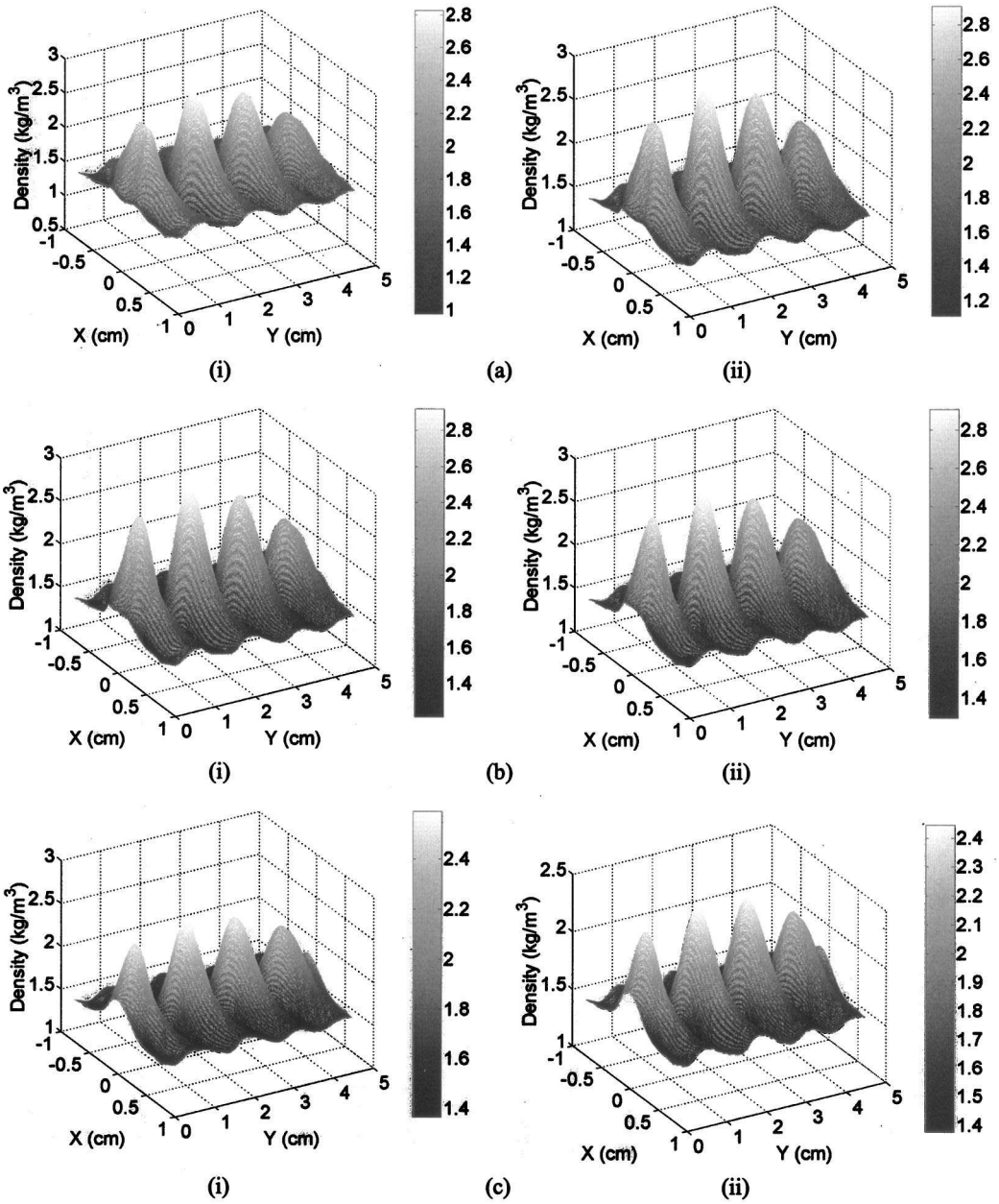

Fig. 8. Reconstructed density distributions in the X–Y planes at distances (a) $z = -0.5$ cm, (b) $z = 0$ cm, and (c) at $z = 0.5$ cm. Data obtained from the phase reconstructed, (i) assuming I = constant and (ii) without the assumption of constant intensity.

umn i) assuming constant transverse intensity and (column ii) without this assumption. The diamond-like cells of higher density can clearly be seen. The value of the maximum density in the cells varied from 2.321 (nearest to the nozzle) to 2.037 kg/m^3 (farthest from the nozzle) for (a) the cross section at $z = -0.5$ cm, from 2.382 to 2.191 kg/m^3 for (b) the cross section at $z = 0$ cm, and from 2.309 to 1.991 kg/m^3 for (c) the cross section at $z = 0.5$ cm. Closer examination of the results of Figs. 8(i) and 8(ii) reveal that fine structures are present near the shock edges in the images obtained without the assumption of uniform transverse intensity as compared with the results obtained with this assumption.

To verify the accuracy of the reconstructed densities, we have carried out an additional experiment with the flow obstructed by a conical structure with a half-cone angle of 30° kept at approximately 3 mm from the nozzle exit. An image of the reconstructed phase is shown in Fig. 9. The oblique shock formed is seen, and the shock angle is measured as approximately 46°. With additional data that the Mach number of the nozzle is 2.9, the density ratio of the regions behind and after the shock is calculated[31] as 2.42. From the experimental result of Fig. 9, this ratio is found to be equal to 2.3.

The major assumption made in this study is the cylindrical symmetry of the flow. The errors due to

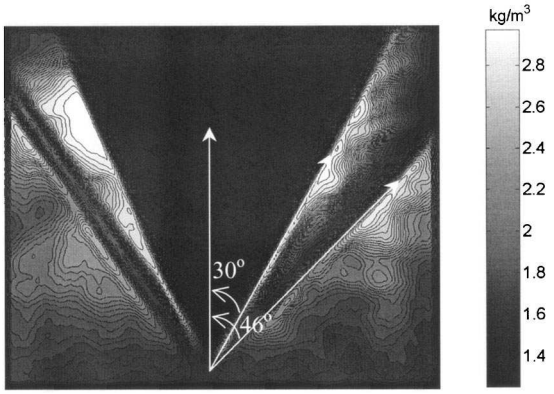

Fig. 9. Result of the experiment done for testing the accuracy of the reconstructions. A conical obstruction of a half-angle of 30° is introduced into the jet, and the density in the vicinity is reconstructed. The reconstructed density in the central plane is shown in the figure. Theoretically the oblique shock angle of 46° obtained with a cone of a half-angle of 30° corresponds to a density ratio of 2.42 across the shock. Tomographic reconstruction gave a density ratio to be approximately 2.3.

this assumption can be avoided if phase data could be gathered for more views. This would call for the use of more cameras and their simultaneous operation.

6. Conclusions

Certain assumptions have been made while we carried out the present analysis, which would have affected the accuracy of the reconstructed density profile. In one of the methods for obtaining the phase data from intensity measurements,[17] the intensity is assumed to be not varying, which is not true in the cases considered here. The reconstructed phase with this assumption appears smoothened when compared with those for which this assumption is not made. In the second method of solving for the phase with the FEM, the intensity profile has been linearly fitted to nodal points to solve for the phase values at these nodal points. These nodal values are interpolated linearly within elements to obtain the phase at any desired point, which is only an approximate solution again. The Fourier-harmonics-based method should give us a more accurate phase reconstruction if Eq. (3), which does not restrict intensity to be constant, is used to get back the Fourier coefficients of the phase.

The 3-D cone-beam algorithm[18] used for reconstructing the refractive-index distribution from the phase data is mathematically accurate only for the reconstruction plane containing the source trajectory of the cone beam (it turns out to be the midplane in the FDK geometry). Other accurate algorithms,[28,29] which give better reconstruction results for the points outside the midplane, at the cost of increased computation complexity, are being implemented. The straight-path assumption of the optical rays is another source of error. A computationally efficient 3-D ray-tracing algorithm, for the modification of the cone-beam reconstruction method, is required for solving this problem, which is under development.

The same set of projection data is used for all the views, which forces circular symmetry on the reconstructions, which need not be the case in the actual flow. In addition, in all the experiments we have assumed that the flow has attained a steady state while the data are gathered. Slight fluctuations from a steady state during data collection would corrupt the reconstruction. For situations in which flow has no circular symmetry, data should be gathered, preferably simultaneously, for a number of views all around the flow.

No attempt is made to correct for refraction suffered by the light ray in traveling through the high-gradient density distribution. Iterative reconstruction methods,[32] using ray tracing to implement forward propagation and the simultaneous algebraic reconstruction technique through curved rays for inversion, are used for refraction-corrected reconstruction of 2-D objects. For 3-D objects, ray tracing is computationally expensive. Such an iterative procedure with a modified cone-beam reconstruction procedure along curved rays is planned for a future study.

References

1. N. Kolmogorov, "A refinement of previous hypotheses concerning the local structure of turbulence in a viscous incompressible fluid at high Reyolds number," J. Fluid Mech. **13,** 82–85 (1962).
2. B. Chhabra and R. V. Jensen, "Direct determination of the $f(\alpha)$ singularity spectrum," Phy. Rev. Lett. **62,** 1327–1330 (1989).
3. C. Meneveau and K. R. Srinivasan, "The multifractal nature of turbulent energy dissipation," J. Fluid Mech. **224,** 429–484 (1991).
4. M. Raffel, H. Richard, and G. E. A. Meier, "On the applicability of background oriented optical tomography for large scale aerodynamic investigations," Expt. Fluids **28,** 477–481 (2000).
5. R. E. Pierson, D. F. Olson, E. Y. Chen, and L. McMackin, "Comparison of reconstruction-algorithm performance for optical-phase tomography of a heated air flow," Opt. Eng. **39,** 838–846 (2000).
6. L. McMackin, B. Masson, N. Clark, K. Bishop, R. Pierson, and E. Chen, "Hartmann wavefront sensor studies of dynamic organized structures in flow fields," AIAA J. **33,** 2158–2164 (1995).
7. A. C. Kak and M. Slaney, *Principles of Computerized Tomographic Imaging* (IEEE Press, New York, 1988).
8. K. Creath, "Phase measurement interferometry techniques," in *Progress in Optics*, E. Wolf, ed. (North Holland, Amsterdam, 1988), pp. 349–392.
9. G. W. Faris and R. L. Byer, "Three-dimensional beam-deflection optical tomography of a supersonic jet," Appl. Opt. **27,** 5202–5212 (1988).
10. G. Keshava Datta and R. M. Vasu, "Non-interferometric methods of phase estimation for application in optical tomography," J. Mod. Opt. **46,** 1377–1388 (1999).
11. J. R. Fienup, "Phase retrieval algorithms: a comparison," Appl. Opt. **21,** 2758–2769 (1982).
12. M. H. Maleki, A. J. Devaney, and S. Alon, "Tomographic reconstruction from optical scattered intensities," J. Opt. Soc. Am. **9,** 1356–1363 (1992).
13. N. Streibl, "Phase imaging by the transport equation of intensity," Opt. Commun. **49,** 6–10 (1984).
14. T. E. Gureyev, A. Roberts, and K. A. Nugent, "Phase retrieval with the transport-of-intensity equation: matrix solution

with use of Zernike polynomials," J. Opt. Soc. Am. A **12,** 1932–1941 (1995).
15. A. Barty, K. A. Nugent, A. Roberts, and D. Peganin, "Quantitative phase tomography," Opt. Commun. **175,** 329–336 (2000).
16. N. Jayshree, G. Keshava Datta, and R. M. Vasu, "Optical tomographic microscope for quantitative imaging of phase objects," Appl. Opt. **39,** 277–283 (2000).
17. T. E. Gureyev and K. A. Nugent, "Phase retrieval with the transport-of-intensity equation. II. Orthogonal series solution for nonuniform illumination," J. Opt. Soc. Am. A **13,** 1670–1682 (1996).
18. L. A. Feldkamp, L. C. Davis, and J. W. Kress, "Practical cone-beam algorithm," J. Opt. Soc. Am. A **1,** 612–619 (1984).
19. H. S. Ko and K. D. Kihm, "An extended algebraic reconstruction technique (ART) for density-gradient projections: laser speckle photographic tomography," Expt. Fluids **27,** 542–550 (1999).
20. M. R. Teague, "Deterministic phase retrieval: a Green's function solution," J. Opt. Soc. Am. **73,** 1434–1441 (1983).
21. G. Vdovin, "Reconstruction of an object shape from the near-field intensity of a reflected paraxial beam," Appl. Opt. **36,** 5508–5513 (1997).
22. M. Schweiger, S. R. Arridge, M. Hiraoka, and D. T. Delpy, "The finite element method for the propagation of light in scattering media: boundary and source conditions," Med. Phys. **22,** 1779–1791 (1995).
23. A. H. Anderson, "Ray tracing for reconstructive tomography in the presence of object discontinuity boundaries: a comparative analysis of recursive schemes," J. Opt. Soc. Am. **89,** 574–582 (1991).
24. A. V. Lakshminarayanan, "Reconstruction from divergent ray data," in Tech. Rep. 92 (Department of Computer Science, State University of New York at Buffalo, 1975).
25. H. Kudo and T. Saito, "Feasible cone beam scanning methods for exact reconstruction in three-dimensional tomography," J. Opt. Soc. Am. A **7,** 2169–2183 (1990).
26. B. D. Smith, "Image reconstruction from cone beam projections: necessary and sufficient conditions and reconstruction methods," IEEE Trans. Med. Imaging **MI-4,** 14–25 (1985).
27. H. K. Tuy, "An inversion formula for cone-beam reconstruction," SIAM J. Appl. Math. **43,** 546–552 (1983).
28. M. Defrise and R. Clack, "A cone-beam reconstruction algorithm using shift-variant filtering and cone-beam backprojection," IEEE Trans. Med. Imaging **13,** 186–195 (1994).
29. F. Noo, M. Defrise, and R. Clack, "Direct reconstruction of cone-beam data acquired with a vertex path containing a circle," IEEE Trans. Image Process **7,** 854–867 (1998).
30. L. A. Shepp and B. F. Logan, "The Fourier reconstruction of a head section," IEEE Trans. Nucl. Sci. **NS-21,** 21–43 (1974).
31. R. H. Sabersky, A. J. Acosta, E. G. Hauptmann, and E. M. Gates, *Fluid Flow: A First Course in Fluid Dynamics* (Prentice-Hall, Englewood Cliffs, N.J., 1999).
32. A. H. Anderson, "A ray-tracing approach to restoration and resolution enhancement in experimental ultrasound tomography," Ultrason. Imaging **12,** 268–291 (1990).